Healable polymer blends: Computational analysis of damage and healing mechanisms

Sun, Yulin; Mishnaevsky Jr., Leon

Published in:
International Journal of Mechanical Sciences

Link to article, DOI:
10.1016/j.ijmecsci.2025.109938

Publication date:
2025

Document Version
Publisher's PDF, also known as Version of record

International Journal of Mechanical Sciences 287 (2025) 109938

Contents lists available at ScienceDirect

International Journal of Mechanical Sciences

journal homepage: www.elsevier.com/locate/ijmecsci

Healable polymer blends: Computational analysis of damage and healing mechanisms

Yulin Sun *, Leon Mishnaevsky Jr.

Department of Wind and Energy Systems, Technical University of Denmark, Roskilde, 4000, Denmark

ARTICLE INFO

Keywords:
Healing
Polymer blends
Damage evolution
Phase separation
Traction–separation law
Crystallinity

ABSTRACT

Healable polymer blends with phase-separated thermoset/thermoplastic (TS/TP) microstructures have gained significant interest for their high potential in sustainable structural applications. To better understand the damage and healing behavior of these materials, an isotropic continuum cohesive damage-healing model specific to the healable TS/TP blends is first presented within the framework of finite element method. Traction–separation laws of cohesive models are integrated into regular finite elements, where damage variables of each element can be achieved by explicit modeling of crack evolution. A parabolic damage evolution law is derived for elastoplastic polycaprolactone (PCL) based on its experimental stress–strain behavior. Temperature-dependent material properties and time-dependent loading are incorporated in the model. The phase change of PCL is characterized by linking its modulus to crystallinity. The proposed model is validated by applying the model prediction for epoxy/PCL blends consisting of epoxy particles and PCL matrix and comparing the results with experimental data in available literature. Representative volume element (RVE) models of epoxy/PCL blends are developed from realistic micrographs through image-based model generation to capture true microstructures. The proposed model provides a good starting basis for understanding the damage and healing mechanisms in healable TS/TP polymer blends.

1. Introduction

Green transition in Europe requires wider use of strong lightweight materials for various applications, such as wind turbine blades, lightweight airplane components [1], or lightweight vehicles [2,3]. Polymer composites are increasingly used in these structures. Lightweight composite structures should endure very high service loads over a long time and require minimum maintenance and repair costs. In particular, it is important for wind turbine blades, made from polymer composites and subjected to complex, random extreme loads over many decades [4]. Ideally, wind turbines should ensure autonomous service with minimum repair and maintenance efforts. Such autonomous self-maintenance and self-repair can be realized with the use of self-healing materials, which are also capable of healing and repairing possible defects formed during the service time. Thus, future polymer-based composites should ensure both high strength to sustain high loads (like extreme winds) and self-repair capability to heal possible defects. Normally, while thermoplastic materials show a potential for healability, thermosets are much stronger and stiffer. In this paper, we consider the potential of thermoset/thermoplastic (TS/TP) blends for the development of structural polymer composites, which are able to sustain high loads and possess self-healing capacity.

In recent decades, various self-healing mechanisms have been reported for polymer composites, which can generally be categorized into two main categories: extrinsic and intrinsic self-healing mechanisms [5]. Extrinsic self-healing, also known as autonomous self-healing, involves the use of a prefilled healing agent within containers embedded in the matrix to repair damage [6–8], while intrinsic self-healing relies on the dynamic/reversible chemical bonds of the matrix to restructure in the presence of external stimuli [9–11]. Extrinsic systems, in the form of capsules or vascular systems, have been incorporated into fiber reinforced polymers (FRP), however, the majority of research on capsule-based healing systems has demonstrated only one single healing occurrence [12–14]. An alternative strategy is to impart the matrix with intrinsic healing capabilities, which can theoretically heal for an infinite amount of time without using a self-healing agent [15–17]. Lu et al. [18] employed noncovalent host–guest linkages to enable effective self-healing properties. Jing et al. [19] developed ultra-tough supramolecular polymers by integrating acid–base ionic pairs into a hydrogen-bonding network. Despite their remarkable self-healing and toughness, their low stiffness (< 1.3 MPa) limits structural applications. To address this, Chen et al. [20] introduced a shape

* Corresponding author.
E-mail address: yulins@dtu.dk (Y. Sun).

https://doi.org/10.1016/j.ijmecsci.2025.109938
Received 5 July 2024; Received in revised form 1 December 2024; Accepted 1 January 2025
Available online 7 January 2025

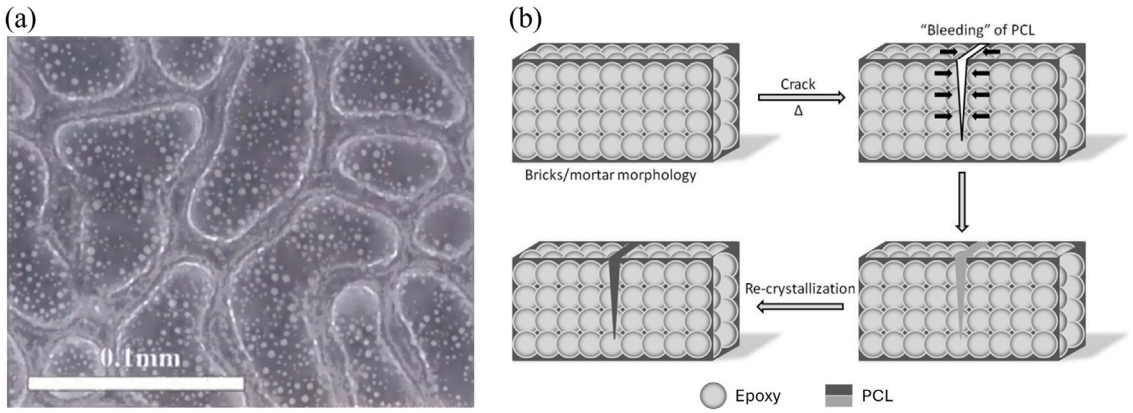

Fig. 1. (a) Typical morphology of epoxy/PCL polymer blends consisting of 25 vol% PCL (epoxy/PCL25) cured at 150 °C (Adapted from Emmerson [26]). (b) Schematic illustration of the overall mechanism of thermal mending in epoxy/PCL polymer blends (Adapted from Luo et al. [22]).

memory polyurea with exceptional energy density, achieved via subtle permanent cross-linking within a hierarchical hydrogen-bonding network, which offers a stiff and tough material with potential for lightweight, high-performance engineering structural matrices.

Another promising approach to provide the matrix with intrinsic healing capabilities involves creating a miscible [21] or immiscible [22] blend between a thermoset matrix and a low melting point semicrystalline thermoplastic. Luo et al. [22] first proposed a type of immiscible TS/TP blends, consisting of epoxy resin and polycaprolactone (PCL), using a simple manufacturing process. This type of TS/TP blends have a "biphasic" structure due to polymerization-induced phase separation (PIPS): (i) a primary "load-bearing" phase characterized by high stiffness and strength, responsible for the main mechanical and structural roles, and (ii) a "healing" phase composed of a thermoplastic healing agent that repairs the material, restoring its mechanical and structural integrity after damage. A typical morphology of epoxy/PCL polymer blends consisting of 25 vol% PCL (epoxy/PCL25) is illustrated in Fig. 1(a). Healing occurs by the flow of melted PCL into the damaged area, where it restores strength upon crystallization, as shown inFig. 1(b). Cohades et al. investigated a similar system over a wider range of compositions [23] and extended the application of phase separated epoxy/PCL blends to a matrix material in FRPs [24]. Furthermore, they explored the potential of shape memory alloy wires to enhance the self-repairing properties [25]. Based on their work on TS/TP polymer blends, the Swiss company CompPair Technology developed and manufactured the healable prepreg HealTech™, which was utilized in liquid composite molding/LCM processes to manufacture a wind turbine blade section. These findings indicate that immiscible TS/TP blends are viable for commercial use and suitable for structural applications.

In order to gain a deeper insight into the phenomenon of self-healing and eventually to prepare self-healing polymeric materials or to modify the healing strategy, computational models are required due to their predictability and guidability [27]. A variety of modeling techniques have been employed to study the damage-healing process in different self-healing materials. The models are typically developed at three different scales: molecular, mesoscale, and continuum. Although molecular dynamics is increasingly used for hierarchical characterizations, computational challenges limit the scales of time, temperature, and length, preventing them from solving many real-world engineering issues [28]. Most mechanical models for studying self-healing behavior are implemented by integrating the healing process into continuum damage mechanics (CDM) models [29,30], fracture mechanics (FM) models [31], or a combination of CDM and FM for damage analysis [32,33].

CDM offers a framework for modeling damage evolution in materials by introducing a damage variable that represents the reduction in load-carrying capacity [34–37]. Do et al. [38] developed a combined continuum damage-embedded discontinuity model which offers higher computational efficiency compared to other strong discontinuity methods. Rong et al. [39] built a novel damage correction formula to model anisotropic plasticity and damage. Wang et al. [40] proposed a modified Lemaitre CDM model to enhance the simulation accuracy of the bonding process in composite plates. To incorporate healing effects, extensive efforts across different levels of complexity have been made to expand CDM into continuum damage-healing mechanics (CDHM). Miao et al. [41] proposed a continuum healing mechanics model within a thermodynamically consistent framework, showing good correlations with experimental data on crushed rock salt and applications to various materials. Then Barbero et al. [42] developed a general CDHM within a consistent thermodynamic framework that automatically satisfies the thermodynamic restrictions and applied it to self-healing fiber-reinforced polymer–matrix composites, where the microcracks were taken as distributed damage, which proved to be able to initiate the release of healing agent from the microcapsules embedded in the matrix of the composites [43]. Numerous researchers have incorporated the CDHM model into their studies. Al-Rub et al. [44] developed a microdamage healing model to enhance the prediction of fatigue life in asphalt mixes. Darabi et al. [45] expanded on the evolutionary laws for microdamage healing discussed in Ref. [44] and introduced a CDM framework to model the healing of microdamage in materials subjected to cyclic loading conditions. Shahsavari et al. [46,47] presented a viscoelastic–viscoplastic constitutive model for self-healing materials, incorporating thermodynamic principles and CDHM. Pan et al. [48] developed a continuum damage-healing model for self-healing materials, using non-equilibrium thermodynamics and phase field method. Voyiadjis et al. [49] proposed a coupled elastoplastic-damage-healing mechanism in a thermodynamic framework for a shape memory polymer based self healing system. Esgandi et al. [50] presented a CDHM model for coupled elastoplastic damage-healing behavior of unsaturated materials. Zhang et al. developed a chemo-mechanically coupled continuum damage-healing theory for transient damage-healing problems of chemical reaction-based self-healing materials [51]. Shojaei et al. [52] proposed a statistical framework to integrate statistical mechanics into CDHM to consider the statistical nature of damage healing mechanics. Ahmed et al. [53] developed a theoretical framework for CDHM by extending stress decomposition to account for tensile, compressive, and shear stresses. To address the limitation in existing CDHM that the healed area cannot undergo damage repeatedly, Subramanian et al. [54–56] introduced a novel secondary damage variable and applied it to elastoplastic and viscoelastic materials. Dai et al. [57] proposed a two-stage modeling and testing framework for characterizing self-healing materials, utilizing a phenomenological healing expression versatile enough to encompass a wide range of engineering materials.

Although the CDHM framework effectively represents the formation and healing of microcracks within a continuum body, it has limitations in simulating crack propagation.

Unlike in CDM, FM deals with structures that contain one or several cracks of finite size. In FM, cracks are usually assumed to be embedded in a non-deteriorating material [58,59]. The extended finite element method (XFEM) provides high accuracy in capturing arbitrary propagating cracks without the need for remeshing, but it faces challenges in handling merging of multiples cracks. The phase-field (PF) model is one of the most high-fidelity methods to simulate microstructure evolution, including crack initiation, branching, and merging, without relying on ad hoc criteria. Kumar et al. [60] developed a healing phase field theory to simulate impact, rebound, and bonding phenomena, but PF suffers from high computational cost. The cohesive zone model (CZM) enables explicit modeling of crack propagation due to its discrete approach to material damage as a cohesive crack, but it has limitations in simulating arbitrary crack paths and is sensitive to mesh size. To incorporate the healing process into FM, research efforts have been made in the literature to model the mechanical behavior of self-healing materials. Maiti et al. [61] utilized a numerical model combining CZM and a contact algorithm to study fatigue crack retardation in self-healing materials, capturing healing kinetics and atomic-scale processes. Abu Al-Rub et al. [62] presented a thermodynamics-based cohesive zone damage-healing model for self-healing materials and introduced a new internal crack healing state variable. Further research was conducted by Alsheghri and Abu Al-Rub et al. [63,64]. Ponnusami et al. [65] proposed a CZM capable of simulating multiple healing events. Jefferson et al. [66] developed a new cohesive damage-healing model for self-healing cementitious materials, which incorporates crack opening displacement and transport of healing agents. Jahadi et al. [67] proposed a novel micromechanics-based damage model for the damage evolution of a two-component microencapsulated-based self-healing polymer composite by pre-inserted interfacial cohesive elements. Xie et al. [68] developed a multiscale fracture mechanics framework for bioinspired staggered heterostructures with self-healing interfaces. Some researchers incorporated XFEM and CZM to simulate interfacial debonding and arbitrary cracks [69–71].

However, most of the existing models focus on capsules or vascular systems and self-healing cement or asphalt materials. Very few computational models have investigated healable phase-separated polymer blends consisting of interconnected thermoset particles within a thermoplastic matrix. This study will focus on the epoxy and PCL polymer blends proposed by Luo et al. [22] and further investigated and industrialized by Cohades et al. [23,25]. The proposed model investigate on both damage and thermal healing mechanisms. To leverage the strengths of both CDM and FM, we presented the cohesive damage-healing model based on the approach proposed by Kurumatani et al. [72], where traction–separation laws are integrated into regular finite elements to calculate the damage variables of CDM.

This manuscript is organized as follows. Section 2 introduces the cohesive damage-healing model for epoxy/PCL polymer blends. First, we describe the damage evolution laws used in the model, followed by a definition of healing variable and a discussion on thermodynamics and crystallization kinetics during the healing process. The selection of the representative volume model size along with the implementation of the finite element model is elaborated in Section 3. Section 4 presents the simulation results and their discussions, highlighting their consistency with the experimental data found in the literature. Finally, we present a summary and draw conclusions in Section 5.

2. Cohesive damage-healing model

In this section, first, the damage evolution laws for epoxy and PCL used in regular finite elements are presented, respectively (Section 2.1). Following that, a thermomechanical model is developed to simulate the thermally activated healing process of epoxy/PCL polymer blends by incorporating a healing variable into the damage model (Section 2.2).

2.1. Isotropic cohesive damage model

To formulate the isotropic damage behavior, we adopted the approach proposed by Kurumatani et al. [72]. In this damage model, the traction–separation laws of the cohesive zone model are integrated into regular finite elements. The scalar damage variable generally used in the continuum damage model [75] can be calculated by explicit modeling of cracks. Furthermore, to minimize the influence of mesh density on mechanical response, the size of the finite element is incorporated as a characteristic length into the damage evolution law, establishing a connection between the crack opening displacement and the strain, as demonstrated by Kurumatani et al. [72]. It should be noted that the epoxy/PCL blends exhibit complex morphologies with irregularly interconnected epoxy particles embedded within a PCL matrix, considering the interfacial strength at the epoxy/PCL (approximately 21 MPa [76]) exceeds the tensile strength of PCL (17.8 MPa), our current model assumes damage occurs only within the epoxy and PCL materials, without accounting for epoxy/PCL interfacial debonding.

2.1.1. Exponential damage model for epoxy

For pure epoxy used in the TS/TP blends, it is a brittle substance that does not exhibit plastic deformation due to high degree of crosslinking density [77]. For damage initiation, the maximum strain criterion is employed. In the damage evolution for epoxy, the exponential softening criterion is employed. The damage variable D for epoxy can be defined as [72]:

$$D(\varepsilon) = 1 - \frac{\varepsilon_0}{\varepsilon} \exp\left(-\frac{E\varepsilon_0 h_e}{G_c}(\varepsilon - \varepsilon_0)\right), \tag{1}$$

where, scalar variable D is called the damage variable that represents the degree of mechanical degradation and takes $0 \leq D \leq 1$. Here, zero means no damage, while 1 corresponds to complete fracture. ε represents the equivalent elastic strain, defined as the maximum elastic principal strain during the loading history. Specifically, it is $\max(\varepsilon_1, \varepsilon_2)$ for 2D cases, and $\max(\varepsilon_1, \varepsilon_2, \varepsilon_3)$ for 3D cases. G_c is fracture energy and ε_0 is the critical strain at which damage initiates. E is Young's modulus. h_e is the length of an element with damage. If $\varepsilon < \varepsilon_0$, the epoxy material remains intact; however, when $\varepsilon \geq \varepsilon_0$, damage occurs and evolves. The engineering stress–strain curve of epoxy used in this study is demonstrated in Fig. 2(a).

2.1.2. Parabolic damage model for PCL

Linear or exponential damage evolution is most commonly used to characterize the rate at which material stiffness is degraded once the corresponding damage initiation criterion is reached. However, from the tensile testing stress–strain response of PCL in Fig. 2(b) obtained by Singh et al. [73], the stress gradually decreases in a manner akin to a parabolic curve once the damage begins. Thus, the parabolic damage evolution is assumed to fit the results of the tensile test of PCL. Although there are some available studies on the evolution of parabolic damage [78,79], they focus primarily on elastic properties. In this study, a new parabolic damage evolution law considering plasticity is developed. The details of formulation are presented in Appendix A. The damage variable for PCL is:

$$D(p) = \frac{4(p - p_0)^2 l_e^2 \sigma_c^2}{9G_t^2}, \tag{2}$$

where p represents the present equivalent plastic strain and p_0 denotes the critical equivalent plastic strain (i.e., failure strain) at which crack initiation occurs. σ_c and G_t represent fracture strength and fracture energy, respectively. l_e is the characteristic length of the element in which the damage is evaluated. By evaluating the magnitudes of p and p_0, we can decide the present status of PCL. Specifically, If $p < p_0$, the PCL material remains intact; however, when $p \geq p_0$, damage initiates and propagates.

Fig. 2(c) illustrates the stress–strain curve for pure PCL as implemented in the numerical analysis. For identical material characteristics,

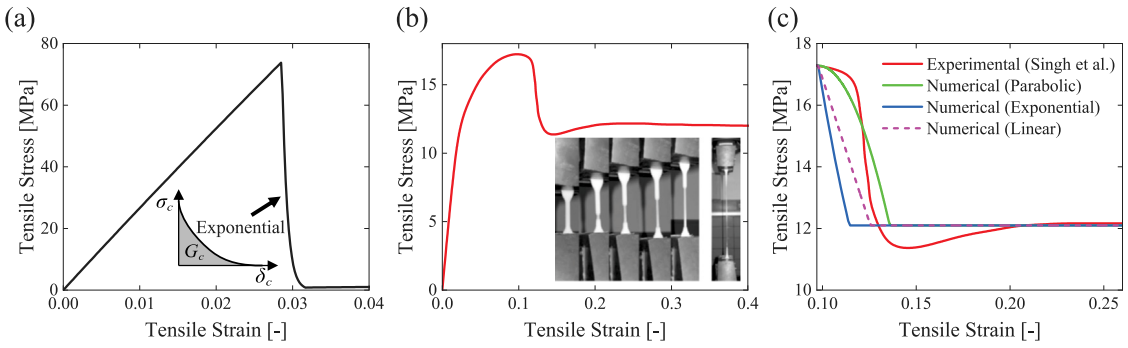

Fig. 2. Engineering stress–strain curves. (a) Stress–strain curve of pure epoxy using exponential damage evolution law. (b) Experimental stress–strain curve of PCL [73] and different moments during the tensile test of PCL [74]. (c) Comparison of numerical and experimental stress–strain curves for PCL during damage evolution process. Parabolic, exponential, and linear damage evolution laws are compared to determine their accuracy in accordance with the experimental data.

the stress–strain curves derived using linear, exponential and parabolic calculations are depicted, respectively. The experimental results in Fig. 2(b) demonstrate that once the yield strength (17.28 MPa) is obtained, a sharp drop in engineering stress is observed to a lower value. From there, stress hardly rises for a large straining interval (up to roughly 400% strain according to and Ref. [74]). Therefore, the damage variable D is limited to a maximum value of 0.3 to align with experimental observations. The parabolic function provides the closest fit to the experimental results when compared to the linear and exponential functions.

2.2. Thermo-mechanical healing model

As mentioned in Section 1, during the healing process of epoxy/PCL25 blends, heating a cracked specimen causes PCL to melt into liquid and flow into the damage zone. Upon cooling, PCL crystallizes to form a hard scar at the crack interface, restoring the mechanical strength of the material. In the experiment, it was observed that differential expansive bleeding (DEB) completes in very short time, shows very little time dependence, and is dominated by heat transfer rather than viscous flow [22]. Therefore, the detailed flow process of the PCL is simplified in the healing model. It is assumed that: (a) the healing model starts at the melting point of PCL; (b) PCL has flown into all damaged elements in epoxy where $D \geq 0.1$ at the beginning of the analytical process; (c) isothermal crystallization is applied during the cooling of PCL.

2.2.1. Heating process

In the healing process, it can be assumed that a damaged element is recovered when PCL flows into the crack. To incorporate the self-healing behavior into the damage constitutive model, a healing variable H [80], ranging from 0 to 1, is generally established according to different healing mechanisms and integrated into the damage variable as:

$$\bar{D} = D(1 - H), \tag{3}$$

where, $\bar{D}$ is the new damage variable in the healing process. The healing variable H ranging from 0 to 1 is defined to characterize the degree of healing, where $H = 0$ means that no damage is healed at the beginning of healing process when there is no PCL flow and $H = 1$ damage is completely healed at the end of PCL flow. The damage variable is assumed to change linearly with flow time of PCL. H is related to the total flow time t_{flow} of PCL, which can be estimated by the overall Kozeny–Carman equation [22]. Thus, the healing variable can be defined as:

$$H = \begin{cases} \frac{\Delta P \Phi_s^2 D_p^2 v^2 t}{150\eta(1-v)^2 L^2}, & \text{if } t < t_{flow} \\ 1, & \text{otherwise} \end{cases}, \tag{4}$$

where, t is current time. ΔP, D_p and Φ_s are expansive pressure, particle size (estimated to be 20 μm from experiments [23], and sphericity (assumed to be 1), respectively. L is the length of the channel and is estimated to be 1 mm, half of the sample "thickness" (normal to the observed surface). η is viscosity of melted PCL. The total flow time t_{flow} of PCL is $\frac{150\eta(1-v)^2 L^2}{\Delta P \Phi_s^2 D_p^2 v^2 t}$ [22]. v is the porosity (void fraction) and can be calculated based on the weight fractions and densities of epoxy and PCL as:

$$v = \frac{\frac{\omega_{PCL}}{\rho_{PCL}}}{\frac{\omega_{PCL}}{\rho_{PCL}} + \frac{\omega_{epoxy}}{\rho_{epoxy}}}, \tag{5}$$

where, ω_{PCL}, ω_{epoxy} are volumetric fractions of PCL and epoxy, ρ_{PCL} and ρ_{epoxy} are densities of PCL and epoxy. For more details of calculation, readers may refer to Ref. [22].

2.2.2. Cooling process

Since the healing model starts from the melted PCL, the internal heat generation can be neglected in the heating process, as no phase transition occurs. However, due to the phase change of PCL from liquid to solid state, it is necessary to account for internal heat generation during the cooling process. The general governing equation for the two-dimensional transient heat transfer problem is:

$$\rho C_p \frac{\partial T}{\partial t} = k_x \left(\frac{\partial^2 T}{\partial x^2} \right) + k_y \left(\frac{\partial^2 T}{\partial y^2} \right) + Q, \tag{6}$$

where, ρ is density, C_p is specific heat, k_x and k_y are coefficients of thermal conductivity in the x- and y-directions, respectively. The volumetric heat source term (Q) represents the internal volumetric heat generation taking place during the phase change of PCL. In this model, it is relevant to rate of crystallinity of PCL and can be expressed as:

$$Q = \rho \Delta H_f \frac{dX_c}{dt}, \tag{7}$$

where, ρ is the density of PCL, ΔH_f corresponds overall enthalpy of 100% crystalline PCL. X_c is the relative crystallinity of PCL and can be obtained by [81]:

$$X_c = \frac{\int_{t_0}^{t_c} (dH_c/dt) dt}{\int_{t_0}^{\infty} (dH_c/dt) dt}, \tag{8}$$

where, t_c is current time. t_0 is the initial crystallization time, and t_∞ is the completion time of crystallization. H_c is the crystallization enthalpy.

The Avrami equation [82–84] has been widely used to characterize the isothermal crystallization kinetics of many polymer systems. The crystallization process of PCL could be described by the Avrami equation as follows:

$$1 - X_c = \exp[-Kt^n], \tag{9}$$

where, X_c is the relative crystallinity, K is the crystallization rate constant in the isothermal crystallization process, and the parameter

n is the Avrami exponent, which determines the crystal geometry and nucleation type. By taking natural logarithms, Eq. (9) can be organized into the following form:

$$\ln[-\ln(1-X_c)] = \ln K - n\ln t. \tag{10}$$

According to Nie et al. [85], there is a linear relationship between $\ln[-\ln(1-X_c)]$ and $\ln t$ for pure PCL. By linear fitting, the values of n and K can be calculated from the slope and intercept of the linear plot of $\ln[-\ln(1-X_c)]$ versus $\ln t$.

The isotropic modulus of PCL at melting point is considered 1000 times lower than the modulus after complete crystallization and the variation of the modulus with the relative crystallinity is assumed to be:

$$E(X_c) = (1-\frac{X_c}{X_c^{max}})E_{\mathrm{m}} + \frac{X_c}{X_c^{max}}E_{\mathrm{c}}, \tag{11}$$

where, X_c^{max} is the maximum relative crystallinity of PCL. E_m and E_c represent the Young's modulus of PCL in the liquid and solid states, respectively. When X_c reaches the maximum crystallinity, the PCL will recover its full stiffness.

For epoxy, it remains solid throughout the temperature range during the healing process. During analysis, the modulus of epoxy decreases with increasing temperature according to experimental observations [23] and is assumed to be linearly temperature dependent.

3. Finite element model

In this section, we first present the image-based model generation process of the finite element model (Section 3.1). Following that RVE models with different dimensions are analyzed to determine the size of RVE to be used (Section 3.2). The implementation of the finite element (FE) model, including the geometry, boundary and loading conditions, material properties, meshing strategy, and solver settings, is then detailed in Section 3.3.

3.1. Generation of geometric models

The reflected light optical microscopy [23] of epoxy/PCL25 blends with 25 vol% PCL (denoted epoxy/PCL25) is used to generate the 2D geometric model. The gathered microstructures come in various resolutions and levels of quality, necessitating preprocessing of the micrographs. In order to obtain the clear phase compositions, the image processing functions of OpenCV python library are utilized. The denoised micrographs are binarized by implementing the adaptive threshold method, which automatically selects a threshold value to segment the epoxy particle and PCL matrix phases. The adaptive threshold of a pixel is set to 1 (in the normalized color range) or 255 (in the 8-bit color range) if its value exceeds the region-based threshold; otherwise, the adaptive threshold is set to zero.

In order to remove the small white blobs in the binarized image, all contours are detected by the built-in function `cv2.findContours` of OpenCV library and thereafter the pixels in the detected small contours are filled with zeros that indicate black color. Geometric features and finite element meshes can be easily generated from the processed 2D binarized image either by open-source codes (e.g. Nanomesh, OOF2, ImageJ, etc.) or commercial software (e.g. image to curve add-in in COMSOL, Im2mesh function in MATLAB, etc.). The schematic of the workflow of finite element modeling based on micrographs is illustrated in Fig. 3.

3.2. Determination of RVE length scale in epoxy/PCL25 blends

An RVE is the minimal material volume that contains enough statistical mechanisms of deformation processes. It should be a volume containing a very large (mathematically infinite) set of microscale elements, possessing statistically homogeneous and ergodic properties [86]. For epoxy/PCL25, the average particle size was measured by Cohades et al. [23] to be around 20 μm.

Taking into account both the model representation and the computational cost, three different sizes of RVEs (50 μm, 100 μm, and 150 μm) are selected to identify the most appropriate RVE size. For each dimension, five different models are analyzed and the Young's modulus is computed for comparison against the tensile test findings of Cohades et al. [23]. Fig. 4 presents a box plot delineating the variability in effective Young's modulus for epoxy / PCL25 polymer blends, across three RVE sizes (50, 100, and 150 μm). Each box represents the interquartile range of the modulus, with the mean value delimited by the central mark. The individual data points are plotted on the boxes, with red indicating the simulated modulus in the x-direction (Sim. E_x) and blue representing the y-direction (Sim. E_y). Furthermore, the dashed lines represent the mean, minimum and maximum experimental moduli reported by Cohades et al. [23] for comparative analysis. Insets depict the typical morphological characteristics of the polymer blends corresponding to each RVE size.

It is observed that the average modulus of the FE models increases with an increase in dimensions, and the scattering of data points reduces with the increase in dimensions. The modulus in the x-direction is similar to that in the y-direction, thus the material can be regarded as homogeneous overall. All data points lie within the limits of the experimental findings; however, they tend to be less than the average value of the experimental data. A primary cause of this inconsistency is the potential misrepresentation of particles in a 3D real sample when approximated in an arbitrary 2D format. This is because the 2D images derived from a sliced 3D sample may not accurately reflect the same microstructural attributes such as area fraction and particle gradation [87]. In this case, the 3D model under examination has a volume ratio of 25% PCL, whereas the 2D sliced model possesses a volume ratio ranging from 33% to 37%. This could clarify why the modulus derived from simulations is less than that acquired from experimental results.

For the sake of ease, as many other studies [69,88–90], we have chosen to use the 2D cross section as a direct representation of the 3D model. To make a trade-off between accuracy and efficiency, a RVE with a dimension of 100 μm is chosen for simulation.

3.3. Implementation of finite element model

The damage and healing phenomena are analyzed within the framework of a continuum theory using the commercial FEM software ABAQUS and its related user subroutines. Five finite element (FE) models, as depicted in Figs. 5 (a)–(b), featuring distinct morphology are established and analyzed. As shown in Fig. 5(a), taking Model 1 as an example, we utilize triangular mesh discretization in the finite element model. The flexibility and irregularity in the arrangement and orientation of triangular elements within the finite element mesh introduces variability in element size and orientation across the mesh, particularly in regions with complex geometries or localized phenomena such as damage initiation and propagation. This allows the mesh to better adapt to complex geometries and dynamic changes, thereby aiding in the accurate capture of the damage evolution and stress distributions. Linear plane stress elements (CPS3) are used for pure damage analysis, while CPS3T elements are employed for healing analysis. The meshes are refined around small geometric features. In the present 2D RVE model, plane stress conditions are assumed. Within a 2D approximation of the epoxy/PCL blend, plane stress conditions are believed to be more appropriate as they correspond to simulating a specimen of

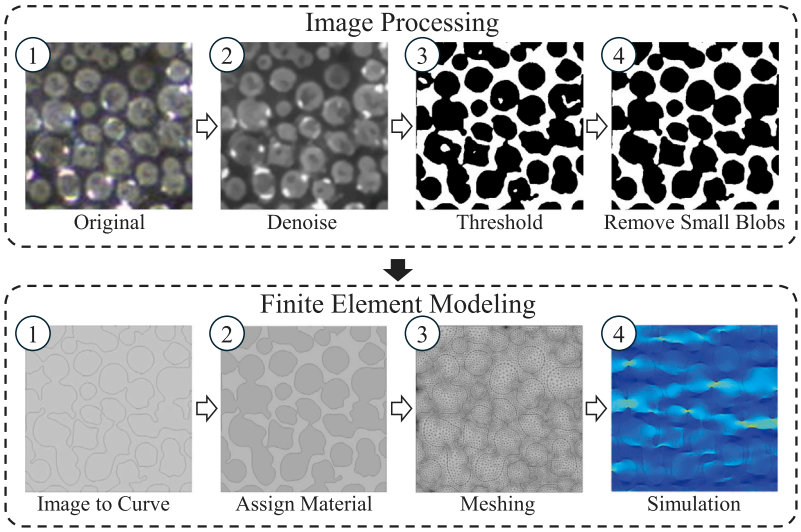

Fig. 3. Workflow of geometrical model generation by micrographs. The geometry models are randomly selected from different locations of the same micrograph for the specimen with 25 vol% PCL obtained in the experiment by Cohades et al. [23] to capture the morphologies of the large micrograph as many as possible.

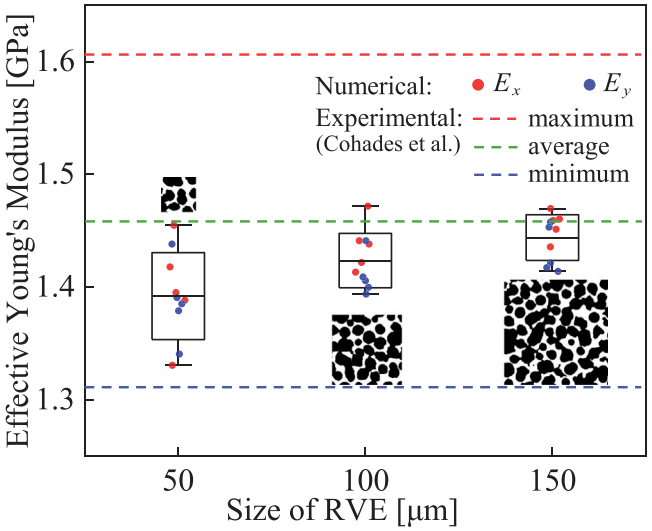

Fig. 4. Numerical and experimental results for the effective moduli of epoxy/PCL25 blends with dimensions of 50 μm, 100 μm, and 150 μm. For each dimension, five RVE models with different morphologies are established and analyzed. All the simulations fall within the range of the maximum and minimum values tested in the experiments by Cohades et al. [23]. Balancing the result dispersion and computational cost, RVEs with a size of 100 μm are chosen.

Table 1
Material parameters for epoxy/PCL25 blends.

Description	PCL	Epoxy
Parameters for material strength		
E (25 °C) [GPa]	0.6 [73]	2.6 [23]
E (150 °C) [GPa]	6×10^{-4}	1.6 [23]
Poisson's ratio	0.3	0.3
G_c [J/m^2]	10	50
Failure strain	0.068 [73]	0.028
Tensile strength [MPa]	17.28 [73]	78 [23]
Parameters for self-healing		
Density [kg/m^3]	1280 [92]	1100 [93]
ΔH_f [J/g]	163 [94]	–
Avrami index	1.93 [94]	–
Crystallization rate constant [min^{-n}]	2.27 [94]	–
Melting point [°C]	60 [23]	–
Viscosity [Pa s]	772.3 [22]	–
Thermal conductivity [W/m K]	0.2 [95]	0.46 [96]
Specific heat [J/kg K]	2000 [97]	1400 [96]
Thermal expansion [K^{-1}]	1.6×10^{-4}	5.44×10^{-5} [98]

small thickness. Under this assumption, it is reasonable that the epoxy particle geometry be constant across the thickness [91]. On the other hand, plane strain conditions imply a large out-of-plane thickness which contradicts the 2D nature of the epoxy/PCL blend geometry.

For the boundary conditions of the FE model in Fig. 5(c), the left boundary is fixed, and symmetry is maintained at the top and bottom boundaries. The right boundary undergoes a loading displacement of 0.01 mm in the x-direction. The FE model is defined without any initial damage. First, damage analysis is implemented in a general static step using implicit solver. The USDFLD subroutine and the GETVRM utility routine in ABAQUS are used to define damage variables and change field-dependent material properties during the analysis. After completing the damage analysis, the stored damage variables of elements are exported and to be used in the healing model. During the healing process, the external tensile load is removed, and a thermal cycle involving heating and cooling is simulated. Thermal-induced residual stress is taken into account. To conduct thermal and stress analysis simultaneously, the implicit coupled temperature–displacement procedure in ABAQUS is utilized. Heat generation defined in Eq. (7) is implemented through the use of HETVAL subroutine. The USDFLD subroutine and the GETVRM utility routine are used to update the damage and healing variables, as well as the material properties. The material parameters used in this model are obtained from available literature [22,23,73,92–98] and the material selection platform Omnexus as given in Table 1.

4. Results and discussion

In this section, we first perform a damage analysis to investigate the mechanical performance of virgin epoxy/PCL25 blends (Section 4.1). Subsequently, the damaged polymer blends undergo a healing process, followed by another damage analysis to assess the mechanical performance of the healed material (Section 4.2).

4.1. Damage model analysis of virgin epoxy/PCL25 blends

Firstly, the influence of maximum damage variable of PCL (as discussed in Section 2.1.2) on the mechanical response of epoxy/PCL25 blends is analyzed in Section 4.1.1. Next, the mechanical performance

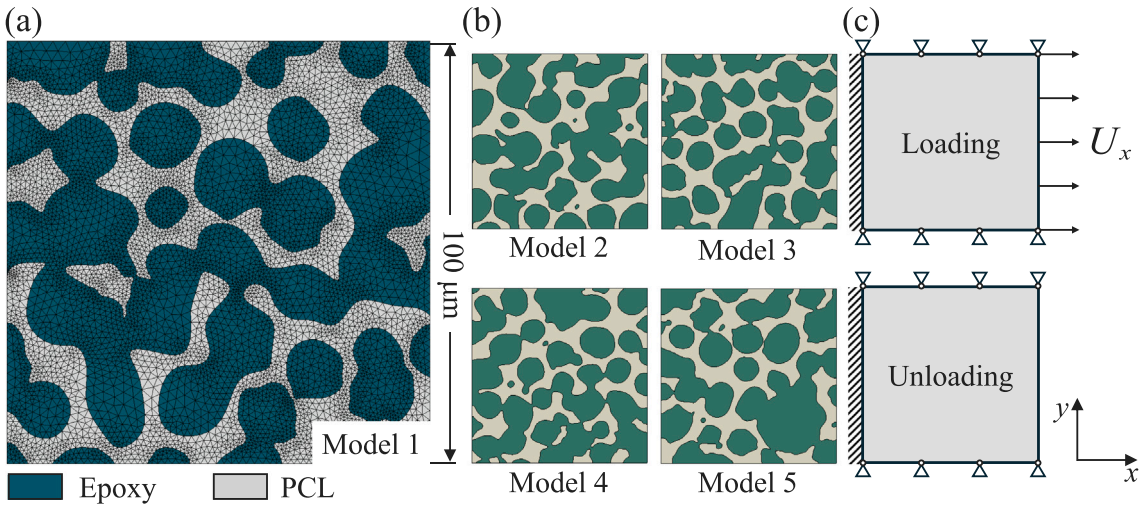

Fig. 5. FE model of epoxy/PCL25. (a) Illustration of mesh generation in Model 1 by plane stress elements CPS3. (b) Geometry of Models 2–5 with different microstructures. (c) Boundary conditions of the FE model. The left boundary is fixed. Symmetry is maintained at the top and bottom boundaries. The right boundary undergoes a loading displacement of 0.01 mm in the x-direction.

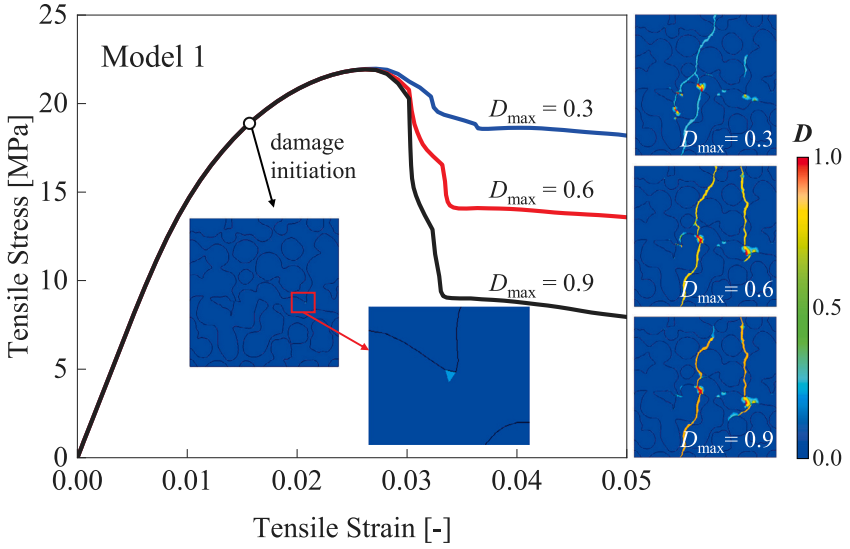

Fig. 6. Influence of maximum damage variables of PCL on overall mechanical response of epoxy/PCL25 blends. Damage initiates at a strain of 0.016. D_{max} = 0.3 fits the experimental stress–strain curve of PCL best. D_{max} = 0.6 and 0.9 are also considered to investigate how different values of D_{max} of PCL affect the overall stress–strain response.

of virgin epoxy/PCL25 is evaluated (Section 4.1.2). Section 4.1.3 demonstrates the damage initiation and evolution of virgin polymer blends.

4.1.1. Parametric study on maximum degradation of PCL

The mechanical characteristics of epoxy/PCL25 blends are investigated. As mentioned in Section 2.1.2, unlike Epoxy, PCL does not reach to complete damage during the damage process, but rather stabilizes at a certain level. To align with the experimental stress–strain curve, the maximum damage variable (D_{max}) for PCL is set at 0.3 instead of 1.0. Considering the variability in testing outcomes for different PCL samples and the discrepancies introduced by different researchers, the maximum damage variable could differ. Consequently, this study explores the impact of D_{max} of PCL on the mechanical properties of the epoxy/PCL25 mixture.

Model 1 has been selected for performing the parametric analysis. Fig. 6 depicts the stress–strain curves for the same FE model and corresponding damage variable distributions with three different D_{max}. The observation reveals that the shapes of the three stress–strain curves are alike, and variations in the maximum damage variable do not significantly influence the peak stress of the polymer blends. The only significant difference is the minimum stress levels after failure.

The contours of the variable damage in Fig. 6 show the damaged area of the same FE model with different D_{max} of PCL in the final loading phase. It is evident from the damage variable contours that the number of cracks grows as the maximum damage variable of PCL increases, however, these three cases exhibit a similar damage pattern. The following simulation only considers the maximum damage variable of 0.3 that fits the stress–strain curve tested by Singh et al. [73].

4.1.2. Mechanical response of virgin epoxy/PCL25 blends

The damage analysis is implemented in the finite element code ABAQUS/standard, an implicit solver, by means of a USDFLD. The average runtime of the computational model is approximately 60 s on a HP workstation with an Intel Core i7-13850HX CPU running Windows 11 Enterprise, 64 bit. Figs. 7(a)–(e) present the stress distributions of the five models under tensile stress when the tensile strain is around 0.035. Fig. 7(f) demonstrates the stress–strain curves for epoxy/PCL25 blends, which shows the mechanical behavior of the five different FE models under tensile loading. Among the five curves, Model 1 and

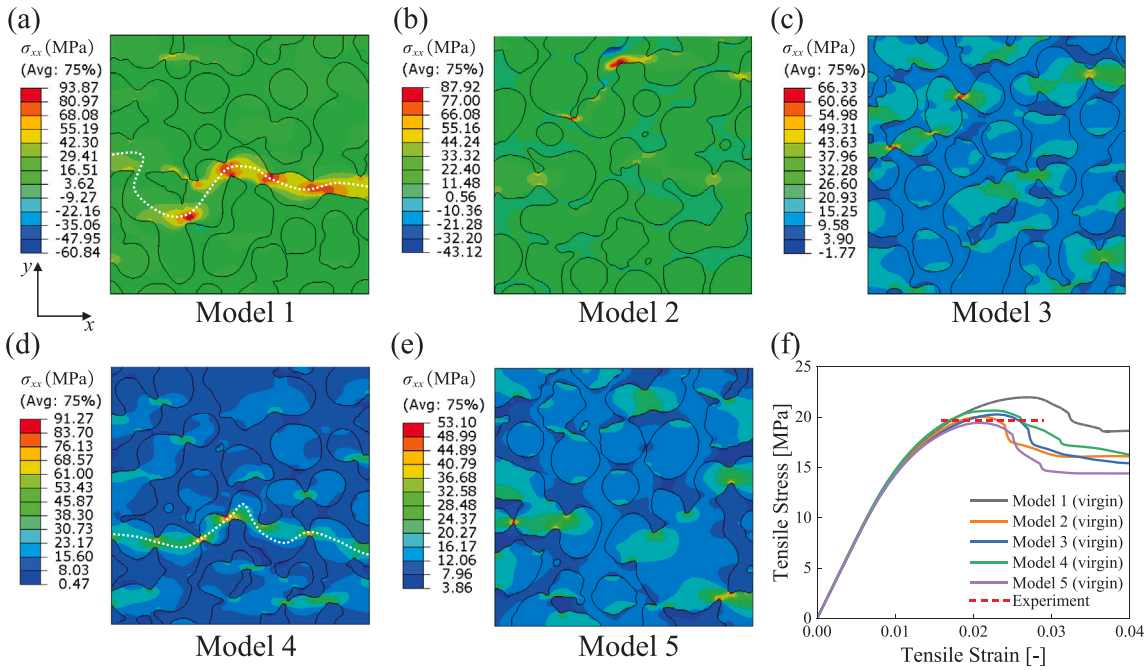

Fig. 7. Mechanical response of virgin epoxy/PCL25 blends. (a)–(e) Stress distribution in tensile direction of Models 1–5 at $\varepsilon = 0.035$. White dotted line in (a, d) marked the fully connected path of interconnected epoxy particles functioning as a primary load-bearing structure. (f) Engineering stress–strain curves for virgin epoxy/PCL25 blends comparing with experimental maximum stress by Cohades et al. [23]. Models 1 and 4 demonstrate the highest strength due to the fully connected path of epoxy particles.

Model 4 exhibit the highest tensile strength. This phenomenon can be explained by the presence of a fully connected network of epoxy particles from left to right in Models 1 and 4, as marked by white dotted lines in Figs. 7(a, d), which functions as the primary load-bearing structure. Since epoxy is stronger than PCL, morphologies such as Models 1 and 4 exhibit higher strength. The ultimate tensile strength reaches around 20 MPa, close to the tensile strength of pure PCL 17.28 MPa (Table 1), which is in agreement with the experimental findings presented in Cohades et al. [23].

In a nut shell, the strength of thermoplastic matrix significantly affects the strength of TS/TP polymer blends. Increasing the strength of the TP matrix will consequently enhance the strength of TS/TP polymer blends. In addition, a higher degree of interconnection among the thermoset particles strengthens the structure.

4.1.3. Damage evolution process

In order to study the damage mechanism in epoxy/PCL25 blends, the numerical results of Model 1 are taken as a representative example. Fig. 8(a) demonstrates the predicted evolution of epoxy and PCL damages in Model 1. Damage initially occurs between epoxy particles at a strain of 0.016 with a stress of 19 MPa, which is above the tensile strength of PCL (17.28 MPa). It can be observed that the damage initiates at the interfaces of interconnected epoxy particles (denoted as Epoxy-Epoxy) and the interfaces between epoxy and PCL (denoted as Epoxy-PCL), and thereafter, damage primarily propagates along the interfaces between epoxy and PCL. This observation is consistent with the results from experiments by Cohades et al. [22,23].

Fig. 8(b) shows the final failure predicted by FE analysis and the snapshots of the fracture morphologies obtained by experiments [23]. From the damage patterns shown in Fig. 8(b), it can be seen that the cohesive failure at interfaces of epoxy particles, as well as between epoxy and PCL can be reasonably predicted by our models, which is approximately consistent with the experimental fracture.

In summary, damage initiates at the interfaces of interconnected epoxy particles (Epoxy-Epoxy) and Epoxy-PCL interfaces, with propagation primarily along the epoxy-PCL interfaces. To improve material performance, future designs should focus on minimizing undesired small features in the interconnected epoxy structure and improving the interfacial strength between thermoset and thermoplastic materials.

4.2. Healing model analysis of damaged epoxy/PCL25 blends

In this section, the mechanical properties of healed epoxy/PCL25 blends are investigated. The model is heated from 60 °C to 150 °C in 270 s, which is between the melting point of PCL and the glass transition of epoxy [23]. This ensures that the epoxy remains in a rigid and solid state and prevents macroscopic softening or flow of the epoxy phase during the heating process, maintaining the structural integrity of the material. At the same time, this temperature is above the melting temperature (T_m) of the PCL phase, allowing the PCL to melt and flow. Upon achieving 150 °C, the model is kept isothermal for 600 s and then quickly cooled to 25 °C in 10 s, followed by an isothermal period of 100 s. The flow time of PCL for 150 °C is calculated according to the overall Kozeny–Carman equation [22], which is approximately 19.9 s for epoxy/PCL25 blends. During the cooling process, the modulus of PCL changes with the relative crystallinity according the to the relationship defined in Eq. (11).

4.2.1. Parametric study on thermal expansion of PCL

During the heating and cooling process, PCL changed from liquid to solid states. The coefficient of thermal expansion (CTE) of PCL can be different in heating and cooling procedures. Typically, the coefficient of thermal expansion rises as the temperature goes up. In this section, taking Model 1 as an example, different values of CTE are considered to assess its influence on mechanical properties.

Figs. 9 (a) and (b) show the residual stress distribution in the blends after healing for different CTE values of melted PCL in Model 1, which corresponds to the CTE used in the heating procedure, because the simulation starts from the melted PCL as mentioned in Section 2.2. It can be observed that higher CTE of melted PCL leads to higher residual stress in the epoxy/PCL25 blends. The maximum stress in Fig. 9(b) is approximately twice as much as that in Fig. 9(a), which aligns with the ratio of the CTE values.

Fig. 9(c) illustrates the stress–strain curves of the healed epoxy/PCL25 blends using different CTE values of melted PCL. The graph reveals that the failure strain of the healed material has a decreasing trend with the increase in the CTE value of melted PCL,

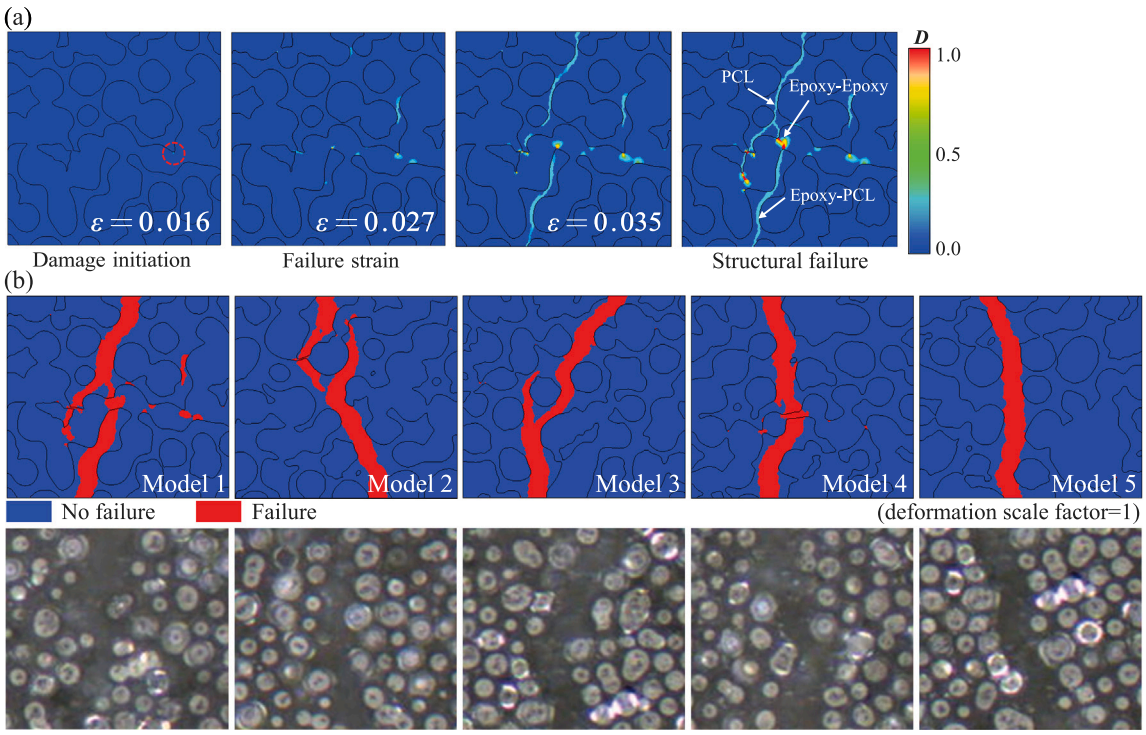

Fig. 8. Damage evolution in virgin epoxy/PCL25 blends. (a) Demonstration of damage variable distribution in Model 1 (deformation scale factor=0). Damage variables from 0 to 1 indicates damage initiation and evolution. Damage primarily propagates along the interfaces between epoxy and PCL. (b) Comparison of fracture morphologies between numerical and experimental results (Micrographs are adapted from Cohades et al. [23]).

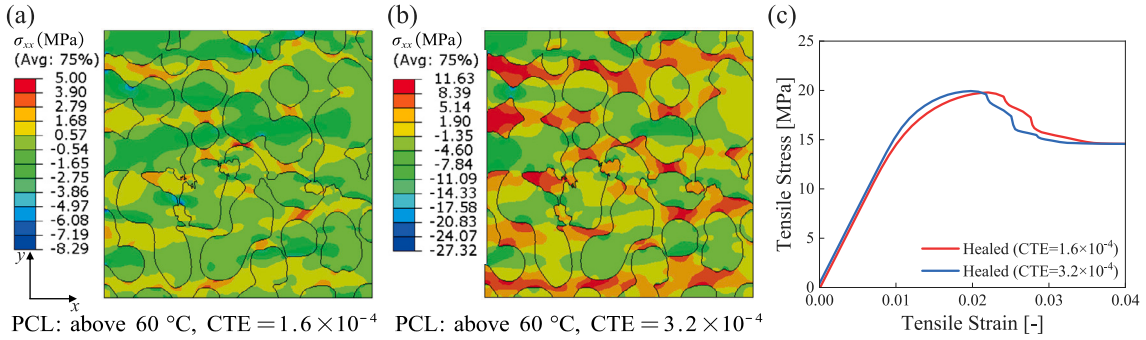

Fig. 9. Residual stress (in tensile direction) of epoxy/PCL25 blends after cooling in Model 1 (deformation scale factor=0): (a) Thermal expansion of PCL above 60 °C is 1.6×10^{-4}; (b) Thermal expansion of PCL above 60 °C is 3.2×10^{-4}. (c) Effects of thermal expansion of PCL on stress–strain response of epoxy/PCL25 blends.

which is attributed to the higher residual stress after cooling when the CTE of melted PCL is higher.

In summary, the coefficient of thermal expansion (CTE) of the melted PCL significantly affects the residual stress in the healed material, which in turn impacts its failure strain; however, it has little effect on the tensile strength of the healed polymer blends. In the following model, we use the CTE value of melted PCL as 3.2×10^{-4}, which is double that of solid-state PCL.

4.2.2. Damage healing in the heating procedure

The healing process of epoxy/PCL25 blends induced by differential expansive bleeding of melted PCL is simplified as elaborated in Section 2.2. The damage variables (D) are modified to implement the damage recovery in the heating process, and the complete damage recovery is achieved when $D = 0$. Taking Model 1 as an example, Fig. 10 demonstrates the damage recovery procedure during heating. In the ideal scenario, PCL would completely heal all the damaged epoxy regions. To account for the possibility of imperfect healing, we introduced a threshold in the healing model: epoxy elements with a damage variable $D < 0.1$ are not healed. These elements represent only a small fraction of the damaged regions. With the threshold, a few small epoxy elements retain some level of damage ($D < 0.1$), which acts as the initial damage in the healed material. Without the threshold, the model assumes that all epoxy elements are fully healed by PCL, resulting in no remaining damage. Initially, any damaged elements in epoxy particles with a damage variable greater than 0.1 are substituted with melted PCL. Subsequently, the damage variables reduce linearly over time within the flow period of PCL. Consequently, some damaged elements of the epoxy particles with $D < 0.1$ (marked with white circles) persist in the healed polymer blends.

Theoretically, if epoxy particles are disconnected, damage would be confined to the epoxy-PCL interface and propagate within the PCL. Following healing by PCL, the material's properties could return to their original state. Conversely, when epoxy particles are interconnected, damage may initiate and spread within the epoxy. After healing, the connection between the epoxy particles is replaced by PCL, which could reduce the tensile strength of the healed material.

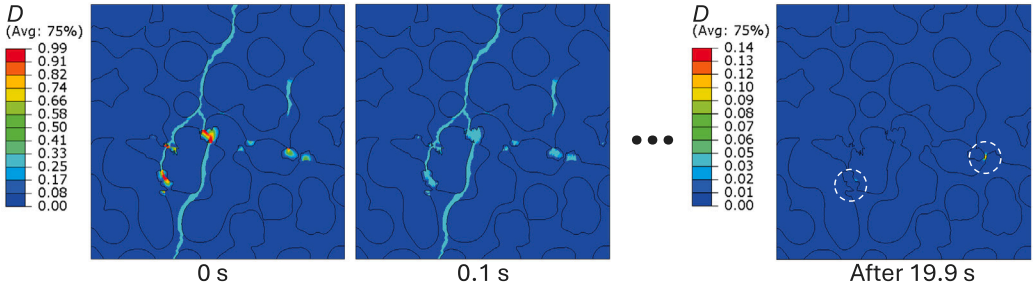

Fig. 10. Damage recovery in the heating process (Model 1). The flow time of PCL is calculated to be 19.9 s. Any damaged elements in epoxy particles with a damage variable greater than 0.1 are assumed to be healed by melted PCL. Consequently, some damaged elements remain unhealed.

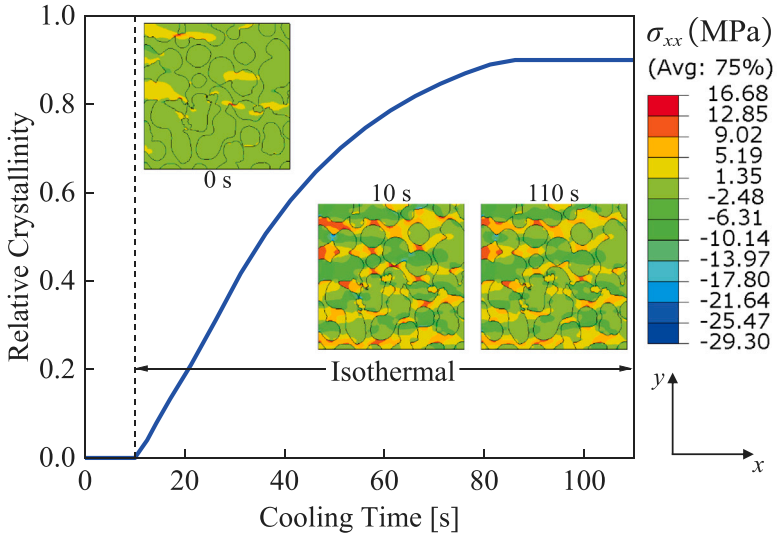

Fig. 11. Relative crystallinity versus cooling time and stress distribution in x−direction. During cooling process, the model is quickly cooled to 25 °C in 10 s, followed by an isothermal period for 100 s. From 0 s to 10 s, thermal stress concentration shifts from epoxy particles to PCL matrix.

4.2.3. Isothermal crystallization of PCL in the cooling procedure

At the end of PCL flow during healing, the healing variable H for elements containing PCL is set to 1, corresponding to a damage variable of zero. Thereafter, the damage and healing variables remain unchanged. During cooling, as the temperature decreases, liquid-state PCL recrystallizes into solid-state PCL, inducing thermal stress. Fig. 11 demonstrates the isothermal crystallization behavior of PCL and corresponding stress contours in x−direction. Since the stress distribution patterns of the five models are alike, we present only the results of Model 1 for the sake of simplicity. It can be observed that at the beginning of cooling, i.e., at the end of heating, the thermal stress concentration occurs in the epoxy particles. After the quick 10 s cooling process, the thermal stress concentration shifts to the PCL matrix. Throughout the isothermal crystallization, the thermal stress concentration is reduced in some regions; however, no significant change can be seen in the overall stress distribution. It is inferable that temperature has a greater influence on the value of residual stress compared to phase changes during crystallization.

4.2.4. Mechanical response of healed epoxy/PCL25 blends

Following the thermal healing process, the healed epoxy/PCL blend is subjected to the same loads as the virgin material (discussed in Section 3.3) to study the mechanical response of the healed material. The healing and re-damage analysis is carried out using a coupled temperature–displacement step in ABAQUS/Standard, with a transient response for the healing process and a steady-state response for the re-damage process. The average runtime of the computational models is approximately 500 s on an HP workstation with an Intel Core i7-13850HX CPU running Windows 11 Enterprise, 64-bit.

Fig. 12(a) shows the stress–strain curves of the five different models for healed material. Models 1 and 4 no longer have the highest strength as shown in the stress–strain curves of the virgin material. This can be explained by Fig. 12(b), which gives the material distribution in virgin and healed epoxy/PCL25 blends for Models 1 and 4. It can be observed that the fully connected network of epoxy particles in Models 1 and 4 are disrupted because the damaged interfaces of epoxy particles are healed by PCL, which leads to a reduction in strength for Models 1 and 4. Fig. 12(c) shows the damage evolution in the healed material of Models 1 and 4. It can be observed that the damage patterns differ from the virgin polymer blends due to the new material distribution.

Fig. 12(d) gives the healing efficiency, which is the ratio of the mechanical properties (Young's modulus, tensile strength, and failure strain) of the healed polymer blends to that of the virgin polymer blends ($P_{\text{healed}}/P_{\text{virgin}}$), for comparison. Unlike Models 1 and 4, the tensile strengths for the healed material in Models 2, 3 and 5 are almost the same as those of the virgin material, since most of the damage occurs in the PCL matrix. Ideally, if the damage is restricted to PCL and is subsequently healed by PCL, the mechanical properties of the healed material should be the same as those of the virgin material. In all simulated models, the healed material shows a lower failure strain compared to the virgin material. The primary cause of lower failure strain might be the thermal residual stress present in the healed material as discussed in Section 4.2.1. In particular, Model 1 (74.0%) and Model 4 (73.9%) show the two lowest failure strain ratios. This could be attributed to distinct morphologies between the virgin and healed structures for Models 1 and 4, because some epoxy elements are healed and replaced with PCL elements, which introduce smaller, sharp features that are prone to stress concentration and large

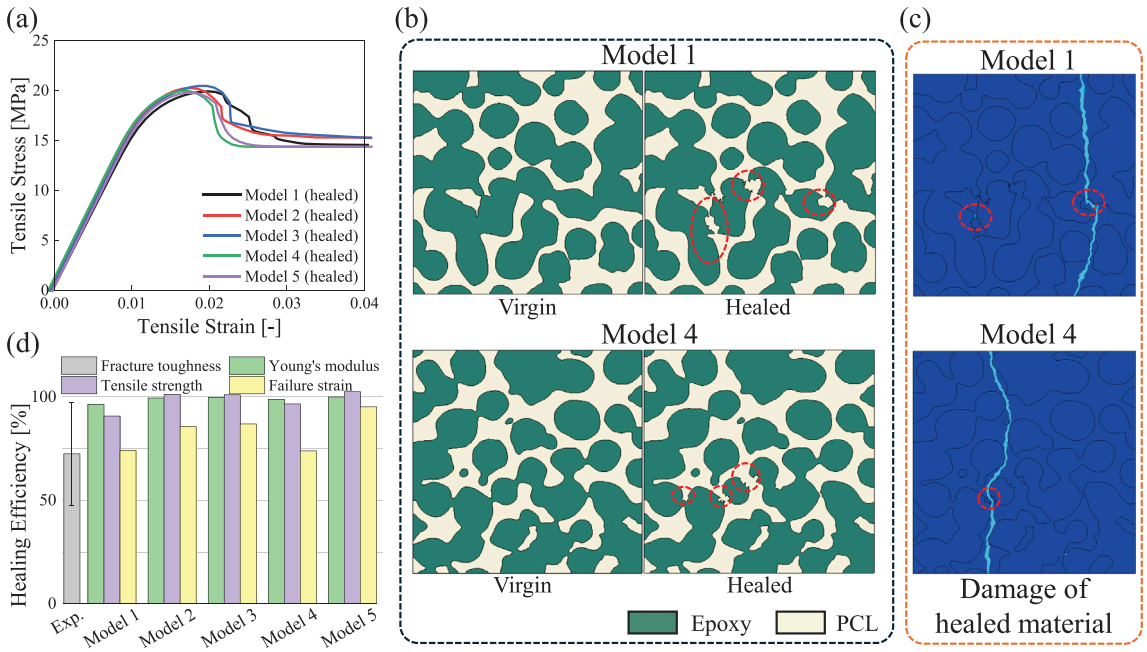

Fig. 12. Mechanical response of healed epoxy/PCL25 blends. (a) Engineering stress–strain curves for healed epoxy/PCL25 blends. Models 2 and 3 demonstrate the highest strength. (b) Material distribution in both the virgin and healed epoxy/PCL25 blends for Models 1 and 4. Damaged epoxy particles are filled and healed by PCL matrix. (c) Damage evolution for Models 1 and 4. Healed zones are re-damaged as indicated by the red circles. (d) Comparison of healing efficiency of healed polymer blends using different indicators. Healing efficiency is obtained by the ratio of the mechanical properties of the healed and that of the virgin polymer blends ($P_{\text{healed}}/P_{\text{virgin}}$), comparing with the experimental result from Cohades et al. [23] using the indicator of fracture toughness.

deformation, potentially making these structures more susceptible to damage compared to the virgin structures. Models 2, 3, and 5 have failure strain ratios of 85.7%, 87.0%, and 95.2%, respectively. For Models 2, 3, and 5, damage primarily occurs within the PCL regions, allowing the microstructure to remain largely consistent before and after healing. The stiffness of the healed material is nearly identical to that of the virgin material. Even in Models 1 and 4, where more regions of damaged epoxy are healed with PCL, there is a slight reduction in stiffness with respective ratios of 96.4% and 99.5%. For comparison, the experimental healing efficiency reported by Cohades et al. [23] is also presented. There is significant scatter in the experimental results. Among the different indicators, the healing efficiency calculated using failure strain shows the closest agreement with the experimental data.

In summary, a fully connected network of epoxy particles that undergo damage and are subsequently healed by PCL leads to a reduction in the overall strength of the structure. Regarding the evaluation of healing efficiency, experimental data suggests that fracture toughness is a reliable indicator. Meanwhile, based on numerical results, failure strain serves as an appropriate indicator, particularly when considering the thermal effects.

5. Conclusions

In this study, a cohesive damage-healing model is presented to investigate the damage and healing performance of thermoset/thermoplastics (TS/TP) self-healing polymer blends. The approach proposed by Kurumatani et al. [72] is employed to integrate traction–separation laws into regular finite elements so that the damage variable that is generally used in continuum damage mechanics can be obtained by explicit modeling of cracks. A new parabolic damage evolution law is developed to fit the experimental results. The healing characteristics are incorporated by coupling the damage variable with a healing variable that is related to the flow time of the thermoplastic matrix.

To validate the proposed model, the predicted damage evolution and tensile strength of virgin epoxy/PCL25 blends are compared against the experimental data by Cohades et al. [23]. A good agreement between the predicted and experimental results demonstrates that the developed model can reliably predict not only the failure behavior in both epoxy and PCL materials but also the overall material properties of the polymer blends. From damage analysis, it has been found that the strength of TS/TP polymer blends can be enhanced by employing high-strength thermoplastics, increasing the degree of interconnection between thermoset particles, or combining both strategies.

Furthermore, a coupled temperature–displacement step is utilized to simultaneously account for both the mechanical and thermal responses during the healing and re-damage processes. A parametric study of the thermal expansion of melted PCL reveals that it significantly impacts the residual stress in the healed material, resulting in a reduced failure strain. Furthermore, numerical results show that temperature variations have a more pronounced effect on residual stress than crystallization-induced phase changes.

It is also notable that interconnected epoxy particles tend to degrade at their interfaces and PCL heals these damaged interfaces, which leads to a decrease in the strength of the healed polymer blends. Therefore, to improve the mechanical properties of TS/TP polymer blends, it is recommended to utilize high-strength thermoplastics and implement strategies to minimize thermal stress during the thermally activated healing process. This approach will help maintain the strength and durability of the healed material.

Overall, this work provides a solid foundation for understanding damage and healing phenomena in self-healing TS/TP polymer blends. However, the computational model requires refinement to account for realistic conditions, including the incorporation of interfacial debonding at TS/TP interfaces to capture detailed damage evolution. Investigating the mechanical response under cyclic loading, including potential hysteresis behavior, will also be crucial. High-fidelity 3D computational models must be developed and validated using experimental data, such as stress–strain testing and 3D micrographs. Future efforts should focus on testing new TS/TP blends with high-performance thermoplastics, advancing 3D microstructure reconstruction techniques, and establishing 3D RVE models.

CRediT authorship contribution statement

Yulin Sun: Writing – review & editing, Writing – original draft, Visualization, Validation, Methodology, Investigation, Formal analysis, Data curation, Conceptualization. **Leon Mishnaevsky Jr.:** Writing – review & editing, Writing – original draft, Supervision, Software, Resources, Project administration, Methodology, Funding acquisition, Data curation, Conceptualization.

Declaration of competing interest

The authors declare that they have no known competing financial interests or personal relationships that could have appeared to influence the work reported in this paper.

Acknowledgments

The authors acknowledge the financial support of the European Commission via Horizon project "Blades2Build: Recycle, Denmark, repurpose and reuse end-of-life wind blades composites: A coupled pre- and co-processing demonstration plant", grant agreement 101096437, and of the Ministry of Foreign Affairs of Denmark via Danida grant 19-M02-DTU "Maintenance and repair strategy for wind energy development" (maintainergy.dk). LM is grateful to the Velux Foundation for its support of the project PREMISE "Preventing MIcroplastics pollution in SEa water from offshore wind".

Appendix A. Formulation of parabolic damage evolution

Fig. A.13 shows the linear, exponential, and parabolic damage evolution laws. In the discussed model, it is assumed that the relationship between the cohesive force and the crack opening displacement (COD) by tensile fracture can be expressed by a parabolic function:

$$\sigma_f = -A\delta^2 + B, \tag{A.1}$$

where σ_f is the cohesive force representing stress transfer on a fracture surface, δ is the COD of the fracture surfaces, and A and B are unknown material parameters.

Denoting the uniaxial tensile strength by σ_c, it can be recognized that σ_f equals σ_c when $\delta = 0$. Then, the parameter B can be expressed as fracture strength σ_c:

$$B = \sigma_c. \tag{A.2}$$

When $\sigma = 0$, $\delta = \delta_c$ (COD at failure), we can obtain that the parameter A can be expressed by

$$A = \sigma_c/\delta_c^2. \tag{A.3}$$

Substitute Eq. (A.2) and Eq. (A.3) into Eq. (A.1):

$$\sigma_f = (1 - \frac{\delta^2}{\delta_c^2})\sigma_c. \tag{A.4}$$

The fracture energy, denoted by G_c, is defined as the energy per unit area required to form a fracture surface, which equals the area under the cohesive force-COD curve as depicted in Fig. A.13. According to this definition, the fracture energy must satisfy:

$$G_c = \int_0^{\delta_c} \sigma_f d\delta = \int_0^{\delta_c} (-A\delta^2 + B)d\delta = -\frac{1}{3}A\delta_c^3 + B\delta_c. \tag{A.5}$$

Substitute Eq. (A.2) and Eq. (A.3) into Eq. (A.5), the maximum COD can be expressed by:

$$\delta_c = \frac{3G_c}{2\sigma_c}. \tag{A.6}$$

Considering plasticity, damage will begin when the equivalent plastic strain p is equal to the critical equivalent plastic strain p_0. For isotropic hardening, the equivalent plastic strain can be obtained by:

$$p = \int \frac{\boldsymbol{\sigma} : d\boldsymbol{\varepsilon}^{pl}}{\sigma_c}, \tag{A.7}$$

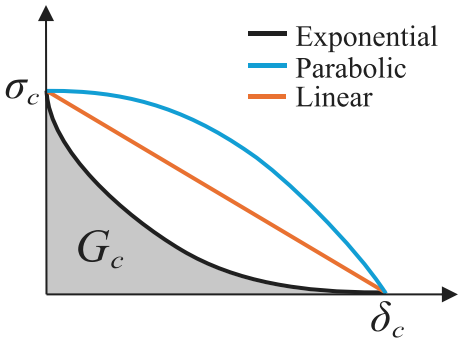

Fig. A.13. Comparison of exponential, linear and parabolic damage evolution laws. σ_c and δ_c denote strength and crack opening displacement at failure, respectively. G_c is fracture toughness.

where $\boldsymbol{\sigma}$ and $\boldsymbol{\varepsilon}^{pl}$ represent Cauchy stress tensor and plastic strain tensor at current state, respectively. Supposing that a single element accommodates a single crack, the COD δ can be expressed as:

$$\delta = (p - p_0)l_e \quad (\text{for } p \geq p_0), \tag{A.8}$$

where δ represents the current crack opening displacement. l_e is the characteristic length of the element in which the damage is evaluated. Here, p represents the present equivalent plastic strain and p_0 denotes the critical equivalent plastic strain (i.e., failure strain) at which crack initiation occurs. In ABAQUS standard, p can be directly obtained from 'PEEQ' using the utility routine GETVRM. The formulation for equivalent plastic strain is:

$$p = \int \dot{p} = \int \sqrt{\frac{2}{3}\dot{\boldsymbol{\varepsilon}}^p : \dot{\boldsymbol{\varepsilon}}^p}, \tag{A.9}$$

where $\dot{p}$ represents equivalent plastic strain rate, and $\dot{\boldsymbol{\varepsilon}}^p$ is rate of plastic flow.

For one dimensional damage model, the stress σ_f can also be described by:

$$\sigma_f = (1 - D)E_0\varepsilon^e, \tag{A.10}$$

where D is damage variable, E_0 is the Young's modulus of the undamaged material, and ε^e represents the present equivalent elastic strain. Combine Eq. (A.4) and Eq. (A.10), the damage variable D can be expressed as follows:

$$D = 1 - \frac{\sigma_f}{E\varepsilon^e} = \frac{\delta^2}{\delta_c^2}\frac{\sigma_c}{E\varepsilon^e} \approx \frac{\delta^2}{\delta_c^2}. \tag{A.11}$$

Substitute Eq. (A.6) and Eq. (A.8) into Eq. (A.11), the relationship between the damage variable and the present equivalent plastic strain can be expressed by:

$$D = \frac{4(p - p_0)^2 l_e^2 \sigma_c^2}{9G_t^2}. \tag{A.12}$$

Data availability

Data will be made available on request.

References

[1] Ghori SW, Siakeng R, Rasheed M, Saba N, Jawaid M. 2 - The role of advanced polymer materials in aerospace. In: Jawaid M, Thariq M, editors. Sustainable composites for aerospace applications. Woodhead publishing series in composites science and engineering, Woodhead Publishing; 2018, p. 19–34. http://dx.doi.org/10.1016/B978-0-08-102131-6.00002-5.

[2] Zhang J, Lin G, Vaidya U, Wang H. Past, present and future prospective of global carbon fibre composite developments and applications. Composites B 2023;250:110463. http://dx.doi.org/10.1016/j.compositesb.2022.110463.

[3] Muhammad A, Rahman MR, Baini R, Bin Bakri MK. 8 - Applications of sustainable polymer composites in automobile and aerospace industry. In: Rahman MR, editor. Advances in sustainable polymer composites. Woodhead publishing series in composites science and engineering, Woodhead Publishing; 2021, p. 185–207. http://dx.doi.org/10.1016/B978-0-12-820338-5.00008-4.

[4] Mishnaevsky Jr. L, Branner K, Petersen HN, Beauson J, McGugan M, Sørensen BF. Materials for wind turbine blades: An overview. Materials 2017;10(11):1285. http://dx.doi.org/10.3390/ma10111285.

[5] Hia IL, Vahedi V, Pasbakhsh P. Self-healing polymer composites: prospects, challenges, and applications. Polym Rev 2016;56(2):225–61. http://dx.doi.org/10.1080/15583724.2015.1106555.

[6] Jahadi R, Beheshti H, Heidari-Rarani M, Navarchian AH. Effect of agitation speed on microencapsulation of healing agent in PMMA shell and study on the mechanical properties of epoxy/PMMA microcapsules. Smart Struct Syst 2021;27(6):1001–10. http://dx.doi.org/10.12989/sss.2021.27.6.1001.

[7] Choi K, Noh A, Kim J, Hong PH, Ko MJ, Hong SW. Properties and applications of self-healing polymeric materials: A review. Polymers 2023;15(22):4408. http://dx.doi.org/10.3390/polym15224408.

[8] Wan P, Wu S, Liu Q, Wang H, Gong X, Zhao Z, et al. Extrinsic self-healing asphalt materials: A mini review. J Clean Prod 2023;425:138910. http://dx.doi.org/10.1016/j.jclepro.2023.138910.

[9] Nik Md Noordin Kahar NNF, Osman AF, Alosime E, Arsat N, Mohammad Azman NA, Syamsir A, et al. The versatility of polymeric materials as self-healing agents for various types of applications: A review. Polymers 2021;13(8):1194. http://dx.doi.org/10.3390/polym13081194.

[10] Li B, Cao P-F, Saito T, Sokolov AP. Intrinsically self-healing polymers: From mechanistic insight to current challenges. Chem Rev 2023;123(2):701–35. http://dx.doi.org/10.1021/acs.chemrev.2c00575.

[11] Mohd Sani NF, Yee HJ, Othman N, Talib AA, Shuib RK. Intrinsic self-healing rubber: A review and perspective of material and reinforcement. Polym Test 2022;111:107598. http://dx.doi.org/10.1016/j.polymertesting.2022.107598.

[12] Li H, Wang R, Liu W. Preparation and self-healing performance of epoxy composites with microcapsules and tungsten (VI) chloride catalyst. J Reinf Plast Compos 2012;31(13):924–32. http://dx.doi.org/10.1177/0731684412442990.

[13] Jin H, Mangun CL, Griffin AS, Moore JS, Sottos NR, White SR. Thermally stable autonomic healing in epoxy using a dual-microcapsule system. Adv Mater 2014;26(2):282–7. http://dx.doi.org/10.1002/adma.201470006.

[14] Yuan L, Huang S, Gu A, Liang G, Chen F, Hu Y, et al. A cyanate ester/microcapsule system with low cure temperature and self-healing capacity. Compos Sci Technol 2013;87:111–7. http://dx.doi.org/10.1016/j.compscitech.2013.08.005.

[15] El Choufi N, Mustapha S, Tehrani B A, Grady BP. An overview of self-healable polymers and recent advances in the field. Macromol Rapid Commun 2022;43(17):2200164. http://dx.doi.org/10.1002/marc.202200164.

[16] Garcia SJ. Effect of polymer architecture on the intrinsic self-healing character of polymers. Eur Polym J 2014;53:118–25. http://dx.doi.org/10.1016/j.eurpolymj.2014.01.026.

[17] Zhong N, Post W. Self-repair of structural and functional composites with intrinsically self-healing polymer matrices: A review. Composites A 2015;69:226–39. http://dx.doi.org/10.1016/j.compositesa.2014.11.028.

[18] Lu P, Xu J, Tian W, Zhang C, Niu S, Zhao J, et al. Robust antifogging coatings with ultra-fast self-healing performances through host-guest strategy. Chem Eng J 2023;465:142868. http://dx.doi.org/10.1016/j.cej.2023.142868.

[19] Jing J, Yao B, Sun W, Chen J, Xu J, Fu J. Ultra-tough, yet rigid and healable supramolecular polymers with variable stiffness for multimodal actuators. Angew Chem Int Ed 2024;n/a(n/a):e202410693. http://dx.doi.org/10.1002/anie.202410693.

[20] Chen J, Wang Z, Yao B, Geng Y, Wang C, Xu J, et al. Ultra-highly stiff and tough shape memory polyurea with unprecedented energy density by precise slight cross-linking. Adv Mater 2024;36(27):2401178. http://dx.doi.org/10.1002/adma.202401178.

[21] Hayes SA, Jones FR, Marshiya K, Zhang W. A self-healing thermosetting composite material. Composites A 2007;38(4):1116–20. http://dx.doi.org/10.1016/j.compositesa.2006.06.008.

[22] Luo X, Ou R, Eberly DE, Singhal A, Viratyaporn W, Mather PT. A thermoplastic/thermoset blend exhibiting thermal mending and reversible adhesion. ACS Appl Mater Interfaces 2009;1(3):612–20. http://dx.doi.org/10.1021/am8001605.

[23] Cohades A, Manfredi E, Plummer CJG, Michaud V. Thermal mending in immiscible poly(ε-caprolactone)/epoxy blends. Eur Polym J 2016;81:114–28. http://dx.doi.org/10.1016/j.eurpolymj.2016.05.026.

[24] Cohades A, Michaud V. Damage recovery after impact in e-glass reinforced poly(ε-caprolactone)/epoxy blends. Compos Struct 2017;180:439–47. http://dx.doi.org/10.1016/j.compstruct.2017.08.050.

[25] Cohades A, Hostettler N, Pauchard M, Plummer CJG, Michaud V. Stitched shape memory alloy wires enhance damage recovery in self-healing fibre-reinforced polymer composites. Compos Sci Technol 2018;161:22–31. http://dx.doi.org/10.1016/j.compscitech.2018.03.040.

[26] Emmerson GT. Phase separation and mechanical properties of epoxy / thermoplastic blends (Ph.D. thesis), Durham University; 2003.

[27] Zhang MQ, Rong MZ. Theoretical consideration and modeling of self-healing polymers. J Polym Sci Part B: Polym Phys 2012;50(4):229–41. http://dx.doi.org/10.1002/polb.22387.

[28] Theodorou DN, Suter UW. Atomistic modeling of mechanical properties of polymeric glasses. Macromolecules 1986;19(1):139–54. http://dx.doi.org/10.1021/ma00155a022.

[29] Oucif C, Voyiadjis GZ, Kattan PI, Rabczuk T. Investigation of the super healing theory in continuum damage and healing mechanics. Int J Damage Mech 2019;28(6):896–917. http://dx.doi.org/10.1177/1056789518799822.

[30] Smojver I, Ivančević D, Brezetić D. Modelling of micro-damage and intrinsic self-healing in unidirectional CFRP composite structures. Compos Struct 2022;286:115266. http://dx.doi.org/10.1016/j.compstruct.2022.115266.

[31] Ozaki S, Osada T, Nakao W. Finite element analysis of the damage and healing behavior of self-healing ceramic materials. Int J Solids Struct 2016;100:307–18. http://dx.doi.org/10.1016/j.ijsolstr.2016.08.026.

[32] Li X, Qu P, Kong H, Zhu Y, Hua C, Guo A, et al. Multi-scale numerical analysis of damage modes in 3D stitched composites. Int J Mech Sci 2024;266:108983. http://dx.doi.org/10.1016/j.ijmecsci.2024.108983.

[33] Hou Y, Wang W, Meng L, Sapanathan T, Li J, Xu Y. An insight into the mechanical behavior of adhesively bonded plain-woven-composite joints using multiscale modeling. Int J Mech Sci 2022;219:107063. http://dx.doi.org/10.1016/j.ijmecsci.2022.107063.

[34] Sharma D, Singh IV, Kumar J. A microstructure based elasto-plastic polygonal FEM and CDM approach to evaluate LCF life in titanium alloys. Int J Mech Sci 2022;225:107356. http://dx.doi.org/10.1016/j.ijmecsci.2022.107356.

[35] Pandey VB, Kuthe N, Mahajan P, Mishnaevsky L. Continuum damage mechanics based computational framework for prediction of the lifetime and degradation of wind turbine coatings with defects. Eng Fail Anal 2023;154:107641. http://dx.doi.org/10.1016/j.engfailanal.2023.107641.

[36] Sun Y, Xing C, Zhang C, Tao C, Ji H, Qiu J. An element-based homogenized model for nonlinear wave interaction with 2D distributed microcracks. Meccanica 2023;58(1):159–77. http://dx.doi.org/10.1007/s11012-022-01626-1.

[37] Fu R, Ling C, Zheng L, Zhong Z, Hong Y. Continuum damage mechanics-based fatigue life prediction of L-PBF Ti-6Al-4V. Int J Mech Sci 2024;273:109233. http://dx.doi.org/10.1016/j.ijmecsci.2024.109233.

[38] Do XN, Reda H, Ganghoffer JF. Impact of damage on the effective properties of network materials and on bulk and surface wave propagation characteristics. Contin Mech Thermodyn 2021;33(2):369–401. http://dx.doi.org/10.1007/s00161-020-00908-x.

[39] Rong H, Hu P, Ying L, Hou W, Dai M. Modeling the anisotropic plasticity and damage of AA7075 alloy in hot forming. Int J Mech Sci 2022;215:106951. http://dx.doi.org/10.1016/j.ijmecsci.2021.106951.

[40] Wang T, Zhao W, Yun Y, Li Z, Wang Z, Huang Q. A dynamic composite rolling model based on Lemaitre damage theory. Int J Mech Sci 2024;269:109067. http://dx.doi.org/10.1016/j.ijmecsci.2024.109067.

[41] Miao S, Wang ML, Schreyer HL. Constitutive models for healing of materials with application to compaction of crushed rock salt. J Eng Mech 1995;121(10):1122–9. http://dx.doi.org/10.1061/(ASCE)0733-9399(1995)121:10(1122).

[42] Barbero EJ, Greco F, Lonetti P. Continuum damage-healing mechanics with application to self-healing composites. Int J Damage Mech 2005;14(1):51–81. http://dx.doi.org/10.1177/1056789505045928.

[43] Barbero EJ, Lonetti P. Application of continuum damage healing mechanics to self-healing composites. In: ASME international mechanical engineering congress and exposition, vol. 37076, 2003, p. 515–9. http://dx.doi.org/10.1115/IMECE2003-43738.

[44] Al-Rub RKA, Darabi MK, Little DN, Masad EA. A micro-damage healing model that improves prediction of fatigue life in asphalt mixes. Internat J Engrg Sci 2010;48(11):966–90. http://dx.doi.org/10.1016/j.ijengsci.2010.09.016.

[45] Darabi MK, Al-Rub RKA, Little DN. A continuum damage mechanics framework for modeling micro-damage healing. Int J Solids Struct 2012;49(3–4):492–513. http://dx.doi.org/10.1016/j.ijsolstr.2011.10.017.

[46] Shahsavari H, Baghani M, Sohrabpour S, Naghdabadi R. Continuum damage-healing constitutive modeling for concrete materials through stress spectral decomposition. Int J Damage Mech 2016;25(6):900–18. http://dx.doi.org/10.1177/1056789515616447.

[47] Shahsavari H, Baghani M, Naghdabadi R, Sohrabpour S. A thermodynamically consistent viscoelastic–viscoplastic constitutive model for self-healing materials. J Intell Mater Syst Struct 2018;29(6):1065–80. http://dx.doi.org/10.1177/1045389X17730914.

[48] Pan Y, Tian F, Zhong Z. A continuum damage-healing model of healing agents based self-healing materials. Int J Damage Mech 2018;27(5):754–78. http://dx.doi.org/10.1177/1056789517702211.

[49] Voyiadjis GZ, Shojaei A, Li G. A thermodynamic consistent damage and healing model for self healing materials. Int J Plast 2011;27(7):1025–44. http://dx.doi.org/10.1016/j.ijplas.2010.11.002.

[50] Esgandani GA, El-Zein A. Thermodynamic based model for coupled elasto-plastic damage-healing behaviour of unsaturated geomaterials. Mech Mater 2020;145:103395. http://dx.doi.org/10.1016/j.mechmat.2020.103395.

[51] Zhang X, Zhu P, Zhong Z. A chemo-mechanically coupled continuum damage-healing model for chemical reaction-based self-healing materials. Int J Solids Struct 2022;236–237:111346. http://dx.doi.org/10.1016/j.ijsolstr.2021.111346.

[52] Shojaei A, Voyiadjis GZ. Statistical continuum damage healing mechanics (SCDHM). Int J Damage Mech 2023;32(6):872–85. http://dx.doi.org/10.1177/10567895231172537.

[53] Ahmed B, Park T, Jeon J-S. Multi-stress damage and healing mechanics in quasi-brittle materials: theoretical overview. Int J Damage Mech 2024;10567895241233833. http://dx.doi.org/10.1177/10567895241233833.

[54] Subramanian H, Mulay SS. On the constitutive modelling of elasto-plastic self-healing materials. Int J Solids Struct 2022;234–235:111289. http://dx.doi.org/10.1016/j.ijsolstr.2021.111289.

[55] Subramanian H, Mulay SS. Constitutive modelling of plastically deformable self-healing materials. Mech Mater 2022;168:104272. http://dx.doi.org/10.1016/j.mechmat.2022.104272.

[56] Subramanian H, Mulay SS. Modelling of self-healing in viscoelastic materials. Int J Solids Struct 2023;270:112235. http://dx.doi.org/10.1016/j.ijsolstr.2023.112235.

[57] Dai Z, Zhu X, Gilabert FA. A multi-material-oriented modeling framework to characterize and predict mechanical self-healing. Int J Mech Sci 2023;260:108644. http://dx.doi.org/10.1016/j.ijmecsci.2023.108644.

[58] Hua W, Li J, Zhu Z, Li A, Huang J, Gan Z, et al. A review of mixed mode I-II fracture criteria and their applications in brittle or quasi-brittle fracture analysis. Theor Appl Fract Mech 2023;124:103741. http://dx.doi.org/10.1016/j.tafmec.2022.103741.

[59] Xing C, Zhou C, Sun Y. A singular crack tip element based on sub-partition and XFEM for modeling crack growth in plates and shells. Finite Elem Anal Des 2023;215:103890. http://dx.doi.org/10.1016/j.finel.2022.103890.

[60] Kumar A, Sajal, Roy P. Peridynamics contact model: Application to healing using phase field theory. Int J Mech Sci 2024;280:109553. http://dx.doi.org/10.1016/j.ijmecsci.2024.109553.

[61] Maiti S, Shankar C, Geubelle PH, Kieffer J. Continuum and molecular-level modeling of fatigue crack retardation in self-healing polymers. J Eng Mater Technol 2006;128(4):595–602. http://dx.doi.org/10.1115/1.2345452.

[62] Abu Al-Rub RK, Alsheghri A. Cohesive zone damage-healing model for self-healing materials. Appl Mech Mater 2015;784:111–8. http://dx.doi.org/10.4028/www.scientific.net/AMM.784.111.

[63] Alsheghri AA, Abu Al-Rub RK. Thermodynamic-based cohesive zone healing model for self-healing materials. Mech Res Commun 2015;70:102–13. http://dx.doi.org/10.1016/j.mechrescom.2015.10.003.

[64] Alsheghri AA, Abu Al-Rub RK. Finite element implementation and application of a cohesive zone damage-healing model for self-healing materials. Eng Fract Mech 2016;163:1–22. http://dx.doi.org/10.1016/j.engfracmech.2016.06.010.

[65] Ponnusami SA, Krishnasamy J, Turteltaub S, van der Zwaag S. A cohesive-zone crack healing model for self-healing materials. Int J Solids Struct 2018;134:249–63. http://dx.doi.org/10.1016/j.ijsolstr.2017.11.004.

[66] Jefferson AD, Freeman BL. A crack-opening-dependent numerical model for self-healing cementitious materials. Int J Solids Struct 2022;244:111601. http://dx.doi.org/10.1016/j.ijsolstr.2022.111601.

[67] Jahadi R, Beheshti H, Heidari-Rarani M. A micromechanical damage-healing model for encapsulation-based self-healing polymer composites under tensile loading. Mech Adv Mater Struct 2024;31(18):4295–308. http://dx.doi.org/10.1080/15376494.2023.2193973.

[68] Xie L, Wu K, Liang X, Song Z, Ding J, Jin J, et al. Toughening by interfacial self-healing processes in bioinspired staggered heterostructures. Int J Mech Sci 2025;285:109847. http://dx.doi.org/10.1016/j.ijmecsci.2024.109847.

[69] Heidari-Rarani M, Asdollah-Tabar M, Mirkhalaf M. Experimental investigation and micromechanics-based damage modeling of tensile failure of polymer concrete reinforced with recycled PET bottles. Eng Fail Anal 2023;148:107197. http://dx.doi.org/10.1016/j.engfailanal.2023.107197.

[70] Hanna J, Elamin A. Computational fracture modeling for effects of healed crack length and interfacial cohesive properties in self-healing concrete using XFEM and cohesive surface technique. Computation 2023;11(7):142. http://dx.doi.org/10.3390/computation11070142.

[71] Taheri-Boroujeni M, Ashrafi MJ. Self-healing performance of a microcapsule-based structure reinforced with pre-strained shape memory alloy wires: 3-D FEM/XFEM modeling. J Intell Mater Syst Struct 2023;34(18):2192–206. http://dx.doi.org/10.1177/1045389X231170163.

[72] Kurumatani M, Terada K, Kato J, Kyoya T, Kashiyama K. An isotropic damage model based on fracture mechanics for concrete. Eng Fract Mech 2016;155:49–66. http://dx.doi.org/10.1016/j.engfracmech.2016.01.020.

[73] Singh NK, Purkayastha BD, Roy JK, Banik RM, Yashpal M, Singh G, et al. Nanoparticle-induced controlled biodegradation and its mechanism in poly(ε-caprolactone). ACS Appl Mater Interfaces 2010;2(1):69–81. http://dx.doi.org/10.1021/am900584r.

[74] Ragaert K, De Baere I, Degrieck J, Cardon L. Bulk mechanical porperties of thermoplastic PCL. In: The 6th polymers & mould innovations international conference. Guimaraes, Portugal; 2014, p. 10–2.

[75] Voyiadjis GZ, Shojaei A. Continuum damage-healing mechanics. In: Voyiadjis GZ, editor. Handbook of damage mechanics: nano to macro scale for materials and structures. New York, NY: Springer; 2021, p. 1–22. http://dx.doi.org/10.1007/978-1-4614-8968-9_46-1.

[76] Simonini L, Canale R, Mahmood H, Dorigato A, Pegoretti A. Multifunctional epoxy/carbon composites with a fully reparable interface. Polym Compos 2024;45(3):2558–68. http://dx.doi.org/10.1002/pc.27939.

[77] Ke J, Li X, Jiang S, Wang J, Kang M, Li Q, et al. Critical transition of epoxy resin from brittleness to toughness by incorporating CO2-sourced cyclic carbonate. J CO2 Util 2018;26:302–13. http://dx.doi.org/10.1016/j.jcou.2018.05.020.

[78] Volokh KY. Comparison between cohesive zone models. Commun Numer Methods Eng 2004;20(11):845–56. http://dx.doi.org/10.1002/cnm.717.

[79] Saikia P, Muthu N. Extrinsic/intrinsic cohesive zone modelling and experiments on interface failure of multi-walled carbon nanotube reinforced adhesively bonded joints under mode II loading. Theor Appl Fract Mech 2023;126:103967. http://dx.doi.org/10.1016/j.tafmec.2023.103967.

[80] Subramanian H, Mulay SS. Continuum damage–healing-based constitutive modelling for self-healing materials: Application to one-dimensional cyclic loading cases. Int J Adv Eng Sci Appl Math 2020;12(1):3–18. http://dx.doi.org/10.1007/s12572-020-00266-6.

[81] Guo Q, Groeninckx G. Crystallization kinetics of poly(ε-caprolactone) in miscible thermosetting polymer blends of epoxy resin and poly(ε-caprolactone). Polymer 2001;42(21):8647–55. http://dx.doi.org/10.1016/S0032-3861(01)00348-2.

[82] Avrami M. Kinetics of phase change. I general theory. J Chem Phys 1939;7(12):1103–12. http://dx.doi.org/10.1063/1.1750380.

[83] Avrami M. Kinetics of phase change. II transformation-time relations for random distribution of nuclei. J Chem Phys 1940;8(2):212–24. http://dx.doi.org/10.1063/1.1750631.

[84] Avrami M. Granulation, phase change, and microstructure kinetics of phase change. III. J Chem Phys 1941;9(2):177–84. http://dx.doi.org/10.1063/1.1750872.

[85] Nie K, Pang W, Zheng S, Wang Y, Lu F, Zhu Q. Non-isothermal crystallization kinetics of poly(ε-caprolactone) in hydrogen-bond-coupled polymeric-inorganic hybrid materials. Polym Int 2005;54(2):327–35. http://dx.doi.org/10.1002/pi.1682.

[86] Gitman I, Askes H, Sluys L, Lloberas-Valls O. The concept of representative volume for elastic, hardening and softening materials. In: Proceedings of XXXII international summer school-conference" advance problems in mechanics. 2004, p. 180–4.

[87] Kim Y-R, Haft-Javaherian M, Castro L. Two-dimensional virtual microstructure generation of particle-reinforced composites. J Comput Civ Eng 2014;30. http://dx.doi.org/10.1061/(ASCE)CP.1943-5487.0000448.

[88] Liang S, Liao M, Tu C, Luo R. Fabricating and determining representative volume elements of two-dimensional random aggregate numerical model for asphalt concrete without damage. Constr Build Mater 2022;357:129339. http://dx.doi.org/10.1016/j.conbuildmat.2022.129339.

[89] Yu J-C, Wang J-T, Pan J-W, Guo N, Zhang C-H. A dynamic FEM-DEM multiscale modeling approach for concrete structures. Eng Fract Mech 2023;278:109031. http://dx.doi.org/10.1016/j.engfracmech.2022.109031.

[90] Tang B, Wang Q, Guo N, Liu J, Ge H, Luo Z, et al. Microstructure-based RVE modeling of ductile failure induced by plastic strain localization in tailor-tempered 22mnb5 boron steel. Eng Fract Mech 2020;240:107351. http://dx.doi.org/10.1016/j.engfracmech.2020.107351.

[91] Palmieri V, De Lorenzis L. Multiscale modeling of concrete and of the FRP–concrete interface. Eng Fract Mech 2014;131:150–75. http://dx.doi.org/10.1016/j.engfracmech.2014.07.027.

[92] Paul D, Varshney A, Mahajan P, Mishnaevsky L. Post-repair residual stresses and microstructural defects in wind turbine blades: computational modelling. Int J Adhes Adhes 2023;123:103356. http://dx.doi.org/10.1016/j.ijadhadh.2023.103356.

[93] Solechan S, Suprihanto A, Widyanto SA, Triyono J, Fitriyana DF, Siregar JP, et al. Investigating the effect of PCL concentrations on the characterization of PLA polymeric blends for biomaterial applications. Materials 2022;15(20):7396. http://dx.doi.org/10.3390/ma15207396.

[94] Qiao X, Li W, Sun K, Xu S, Chen X. Isothermal crystallization kinetics of silk fibroin fiber-reinforced poly(ε-caprolactone) biocomposites. Polym Int 2009;58(5):530–7. http://dx.doi.org/10.1002/pi.2563.

[95] Tian H, Wu F, Chen P, Peng X, Fang H. Microwave-assisted in situ polymerization of polycaprolactone/boron nitride composites with enhanced thermal conductivity and mechanical properties. Polym Int 2020;69(7):635–43. http://dx.doi.org/10.1002/pi.6000.

[96] Ali AM, Jaber MA, A. TN. Mechanical and thermal properties of polyurethane/epoxy IPN's. J Sci Eng Res 2020;7(5):16–9.

[97] Skoglund P, Fransson Å. Continuous cooling and isothermal crystallization of polycaprolactone. J Appl Polym Sci 1996;61(13):2455–65.

[98] Fasanella N, Sundararaghavan V. Atomistic modeling of thermomechanical properties of SWNT/Epoxy nanocomposites. Modelling Simul Mater Sci Eng 2015;23(6):065003. http://dx.doi.org/10.1088/0965-0393/23/6/065003.